CFD simulations of hydrodynamic characteristics in a gas–liquid vertical upward slug flow

Donghong Zheng, Xiao He, Defu Che *

State Key Laboratory of Multiphase Flow in Power Engineering, Xi'an Jiaotong University, Xi'an 710049, China

Abstract

Computational fluid dynamics (CFD) simulations are conducted using the volume-of-fluid (VOF) method to investigate the hydrodynamic characteristics of slug flow and the mechanism of slug flow induced CO_2 corrosion. The hydrodynamic characteristics are significantly affected by the viscous, interfacial, and inertial forces. In inertia dominated flows, the velocity of fully developed falling liquid film is increased with increased Taylor bubble rising velocity. The developing falling liquid film is formed at about the length of 0.5 diameter from the Taylor bubble nose, the fully developed falling liquid film is reached at about the length of 1.5–2.1 diameter from the Taylor bubble nose. The average mass transfer coefficient in the falling liquid film is always higher than that in the Taylor bubble wake zone. The iron ion near wall mass transfer coefficient is higher than that of hydrogen ion. The wall shear stress is increased with increased Taylor bubble rising velocity in fully developed falling liquid film zone, and the wall shear stress has a large fluctuation due to the chaotic and turbulent vortexes in Taylor bubble wake zone. The formation and the damage mechanism of the corrosion product scale are proposed for the gas–liquid two-phase vertical upward slug flow induced CO_2 corrosion. It is found that the wall shear stress of upward gas–liquid slug flow is alternate with high frequency, which is the key factor resulting in the corrosion product scale fatigue cracking. The CFD simulation results are in satisfactory agreement with previous experimental data and models available in literature.
© 2007 Elsevier Ltd. All rights reserved.

Keywords: Gas–liquid slug flow; Hydrodynamic characteristics; Computational fluid dynamics; Flow induced corrosion

1. Introduction

An important consideration in oil and gas industry is multiphase transportation from remote wells for much more economical transport of oil and gas combined. The use of carbon steel or low alloy steel may offer considerable capital savings over the more expensive alloys. However, the frequently encountered multiphase fluids may contain significant levels of CO_2 or H_2S, which in combination with free water can make the pipeline environment seriously corrosive, resulting in the flow induced corrosion, thus the damage to the interior of carbon steel pipe walls, and the decrease in pipe lifetime and even possible shut down of the pipeline. Though CO_2 corrosion and H_2S corrosion have been widely studied in the field and laboratory, and great endeavor has been devoted to the solution of this difficult problem, how to effectively control flow induced corrosion is still challenging scientists and engineers. In the flow induced corrosion, it is found that three causes, namely the mass transfer, the wall shear stress and the electrochemical corrosion, are strongly coupled, and the contribution of individual cause to corrosion cannot be distinguished easily, making this kind of research more complex.

Corrosion is a surface damage process. What is happening near the tube wall has a great influence on the corrosion [1]. The mass transfer coefficient and wall shear stress are the crucial parameters governing the two-phase flow induced corrosion, and the mass transfer and the momentum transfer are intimately related to the diffusion boundary layer

---
* Corresponding author. Tel.: +86 29 82665185; fax: +86 29 82668703.
E-mail address: dfche@mail.xjtu.edu.cn (D. Che).

Nomenclature

c_μ, $c_{\varepsilon 1}$, $c_{\varepsilon 2}$ turbulence model constants, 0.09, 1.44, 1.92

D diameter of pipe, m

D_d diffusion coefficient, m²/s

Eo Eötvös number, $\rho_L g D^2 / \sigma$

Fr_{TB} Froude number, $U_{TB}/(gD)^{0.5}$

k turbulent kinetic energy, m²/s²

k_d mass transfer coefficient, m/s

L characteristic length, m

Mo Morton number, $g(\mu_L)^4/(\rho_L \sigma^3)$

N_f dimensionless inverse viscosity number, $\rho_L(gD^3)^{0.5}/\mu_L$

$\tilde{\mathbf{n}}$ unit normal stress, Pa

P pressure, Pa

r curvature radius, m

Re Reynolds number, uL/v

Sc Schmidt number, v/D_d

t time, s

T absolute temperature, K

$\mathbf{u}$ vector velocity, m/s

u_τ friction velocity, m/s

u^+ normalized turbulent velocity

U axial velocity, m/s

V radial velocity, m/s

x axial distance from the Taylor bubble nose, m

y radial distance from the wall, m

Greek symbols

α volume fraction

μ dynamic viscosity, Pa s

μ^t turbulent eddy viscosity, Pa s

v kinematic viscosity, m²/s

ρ density, kg/m³

σ surface tension, N/m

σ_k Prandtl number for turbulent kinetic energy, 1.0

σ_ε Prandtl number for dissipation rate of turbulent kinetic energy, 1.3

κ Von Karman constant, 0.42

Π_k, Π_ε user defined source terms for turbulent kinetic energy and its dissipation rate

δ thickness, m

ε dissipation rate of turbulent kinetic energy, m²/s²

τ_w wall shear stress, Pa

Subscripts

f   falling liquid film

G   gas phase

L   liquid phase

p   penetration distance of falling liquid film

TB   Taylor bubble

w   wall

k   the kth phase fluid

and the hydrodynamic boundary layer. Therefore, both boundary layers have profound effects on the mass transfer of corrosion reaction species from the bulk solution to the metal substrate and the mass transfer of corrosion products from the metal substrate to the bulk solution. Moreover, they also have significant effects on the electrochemical corrosion reaction rate controlled by diffusion and/or by electrochemical reaction, and on the formation, damage, repair of corrosion product scale.

Due to the limited understanding on the flow induced corrosion mechanism behind gas–liquid two-phase flow, there is an urgent need for a better insight into the details of upward slug flow hydrodynamic characteristics to understand the mechanism of gas–liquid slug flow induced corrosion. Computational fluid dynamics (CFD) technology is a good tool for simulating the hydrodynamic characteristics in a gas–liquid vertical upward slug flow. One of the main merits for CFD is that it can get a deeper insight into the underlying physical mechanisms and thus foster the understanding on gas–liquid two-phase flows; and the other is that it can also provide a unique velocity field and phase distribution with high spatial and temporal resolution for engineering flow applications, which can

hardly be done by today's most advanced experimental techniques.

For a gas–liquid two-phase slug flow, the main complicating feature, which distinguishes from single phase flows, is the existence of deformable interfaces whose shape and distribution are of critical importance in determining the characteristics of the flow. Nevertheless, great progress has been made in the development of advanced numerical methods for simulation of gas–liquid flows with deformable interfaces. The volume-of-fluid (VOF) method originally developed by DeBar [2], Hirt and Nichols [3], and Noh and Woodward [4] can track the motion of gas–liquid boundary using a transport equation for volume fraction occupied by each phase, which is suitable for the simulation involving two immiscible fluids, and can be used to accurately predict the shape of the interface between the fluids.

In this paper, the hydrodynamic characteristics of gas–liquid vertical upward slug flow and the mechanism of slug flow induced CO_2 corrosion are systematically analyzed by CFD numerical simulations using VOF method. These characteristics include the shape of the Taylor bubble, the terminal velocity and thickness of falling liquid film, the

shape and the length of the wake vortexes, the near wall mass transfer and wall shear stress, the slug flow induced CO_2 corrosion rate, the formation and the damage mechanism of corrosion product scale.

2. CFD model development

2.1. Governing equations

Vertical upward gas–liquid two-phase slug flow is characterized by pseudo-periodical alternation of Taylor elongated bubble with an annular falling liquid film around it and a portion of liquid slug, simply described as a sequence of 'slug unit'.

In a slug unit, when a single Taylor bubble with a constant velocity U_{TB} flows upward relative to the tube wall in an inertial coordinates system, the Navier–Stokes momentum equation must be solved as unsteady time-dependent equation. On the other hand, when a reference frame is attached to the rising Taylor bubble, the Taylor bubble becomes stationary and the tube wall moves downwards with the velocity U_{TB}, and the Navier–Stokes momentum equation can be easily solved [5]. Therefore, in the CFD simulations, a reference frame attached to the rising Taylor bubble is used. Since the gas phase is of much lower density and viscosity than the liquid phase, which leads to the condition approximating full slip at the interface between liquid and gas, the circulatory flow of the gas within the Taylor bubble is of little consequence on the outer liquid flow field, and the curve interface is a surface of zero interfacial shear stress [6]. Therefore, the pressure change within the Taylor bubble is very small and can be taken to be uniform constant pressure on the gas phase side of the interface in correspondence with experimental evidence [5,6].

The VOF formulation relies on the fact that two-phase fluids are not interpenetrating and a phase indicator function of the kth phase $\alpha_k(t, \mathbf{r})$ based on the volume fraction, which marks the kth phase fluid position when the fluid moves through the fixed mesh, is tracked. $\alpha_k(t, \mathbf{r})$ is the function of time, t, and space, $\mathbf{r}$, defined as the ratio of the volume of the kth phase in the computational cell to the volume of the computational cell. The function $\alpha_k(t, \mathbf{r})$ is evaluated on the discrete grid as a volume average, for computational cell i, as follows:

$$\alpha_k|_i = \frac{1}{V_i} \int \alpha_k(t, \mathbf{r}) \, dV_i \qquad (1)$$

where $\alpha_k = 1$ means the computational cell full of the kth phase, $\alpha_k = 0$ the computational cell void of the kth phase, $0 < \alpha_k < 1$ the computational cell partially full of the kth phase and containing the gas–liquid interface. The tracking of the phase indicator function α_k and the identification of the location and shape of the interface between the gas–liquid phases are accomplished by solving the volume fraction continuity equation for each phase, expressed as [3]

$$\frac{\partial \alpha_k}{\partial t} + u_j \frac{\partial \alpha_k}{\partial x_i} = 0 \qquad (2)$$

and the volume fractions of all phases sum to unity in each control volume

$$\sum \alpha_k = 1 \qquad (3)$$

The properties of the kth phase are used in the transport equations when the computational cell is completely controlled by the kth phase. At the interface between the phases, the mixture properties are determined based on the volume fraction weighted average, and the density and dynamic viscosity can be expressed as

$$\rho = \sum \alpha_k \rho_k \qquad (4)$$

$$\mu = \sum \alpha_k \mu_k \qquad (5)$$

One set of continuity equation and Navier–Stokes momentum equation describing the motion of the unsteady, viscous, immiscible two-phase flow system for all fluids can be expressed as

$$\frac{\partial (\alpha_k \rho_k)}{\partial t} + \nabla \cdot \alpha_k \rho_k \mathbf{u}_k = 0 \qquad (6)$$

$$\frac{\partial}{\partial t} \alpha_k \rho_k \mathbf{u}_k + \nabla \cdot (\alpha_k \rho_k \mathbf{u}_k \mathbf{u}_k) = -\alpha_k \nabla P + \nabla \cdot \alpha_k \overline{\overline{\tau_k}} + \alpha_k \rho_k \mathbf{F}_k \qquad (7)$$

For a Taylor bubble rising in a flowing liquid of high Reynolds numbers, the standard high Reynolds number k–ε model is valid for the bulk solution. The turbulent kinetic energy k and its dissipation rate ε obey their own transport equation

$$\frac{\partial}{\partial t_k} \alpha_k \rho_k k_k + \nabla \cdot \alpha_k \rho_k \mathbf{u}_k k_k$$
$$= \nabla \cdot \left[\left(\mu_k + \frac{\mu_k^t}{\sigma_k} \right) \nabla k_k \right] + G_k - \alpha_k \rho_k \varepsilon_k + \prod_{k_k} \qquad (8)$$

$$\frac{\partial}{\partial t_k} \alpha_k \rho_k \varepsilon_k + \nabla \cdot \alpha_k \rho_k \mathbf{u}_k \varepsilon_k$$
$$= \nabla \cdot \left[\left(\mu_k + \frac{\mu_k^t}{\sigma_\varepsilon} \right) \nabla \varepsilon_k \right] + \frac{\varepsilon_k}{k_k} (c_{\varepsilon 1} G_k - c_{\varepsilon 2} \alpha_k \rho_k \varepsilon_k) + \prod_{\varepsilon_k} \qquad (9)$$

where

$$\mu_k^t = \frac{c_\mu \rho_k k_k^2}{\varepsilon_k} \qquad (10)$$

$$G_k = \mu_k^t \left(\frac{\partial u_i}{\partial x_j} + \frac{\partial u_j}{\partial x_i} \right) \frac{\partial u_i}{\partial x_j} \qquad (11)$$

$$\sigma_k = 1.0, \quad \sigma_\varepsilon = 1.3, \quad c_\mu = 0.09, \quad c_{\varepsilon 1} = 1.44, \quad c_{\varepsilon 2} = 1.92.$$

The semi-empirical wall function formulation is used to bridge the viscosity affected layer between the wall and the fully turbulent layer.

No boundary condition on interface slip is specified in the VOF model, therefore the gas and liquid phases share a common velocity field, and the interface velocity is not

directly calculated, but rather determined through interpolation of neighboring velocities. If the surface tension force overwhelms the viscous force at the interface, the jump condition at the interface is better satisfied. Surface tension effects are included in the model via the continuum surface force (CSF) of Brackbill [7], which is added into the VOF calculation results in an additional source term in the momentum equation. At the interface between gas and liquid, the viscous effect is neglected and the surface tension coefficient is assumed to be constant. The pressures difference in the two fluids on either side of the interface can be expressed by Laplace's formula

$$p_L - p_G = \sigma \kappa \tag{12}$$

where κ is the curvature defined in terms of the divergence of the unit normal stress $\tilde{\mathbf{n}}$

$$\kappa = \nabla \cdot \tilde{\mathbf{n}} \tag{13}$$

$$\tilde{\mathbf{n}} = \frac{\mathbf{n}}{|\mathbf{n}|}, \quad \mathbf{n} = \nabla \alpha_G \tag{14}$$

The continuum surface force can be written in terms of the pressure jump across the interface. The force at the interface can be expressed as a volume force using the divergence theorem. In gas–liquid two-phase flow, the volume force can be expressed as

$$\mathbf{F}_{vol} = \sigma \frac{2\rho \kappa \nabla \alpha_G}{(\rho_G + \rho_L)} \tag{15}$$

where ρ is calculated by Eq. (4).

According to the Chilton–Colburn analogy, the mass transfer coefficient k_d is proportional to the $(\tau_w/\rho)^{0.5}$ and can be expressed as follows:

$$k_d = C \times \left(\frac{\tau_w}{\rho}\right)^{0.5} Sc^{2/3}, \quad Sc > 100 \tag{16}$$

where C is a constant value.

Dayalan [8] proposed a carbon dioxide corrosion mechanistic model, and the overall corrosion process can be divided into four steps as follows:

(1) Formation of reactive species in the bulk solution

$$CO_2 + H_2O \leftrightarrow H_2CO_3 \tag{17}$$
$$H_2CO_3 \leftrightarrow HCO_3^- + H^+ \tag{18}$$
$$HCO_3^- \leftrightarrow CO_3^{2-} + H^+ \tag{19}$$

(2) Transportation of reactants from the bulk solution to the metal substrate surface

$$H_2CO_3(bulk) \rightarrow H_2CO_3(surface) \tag{20}$$
$$HCO_3^-(bulk) \rightarrow HCO_3^-(surface) \tag{21}$$
$$H^+(bulk) \rightarrow H^+(surface) \tag{22}$$
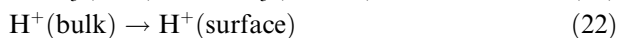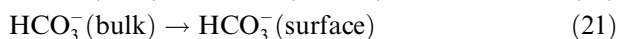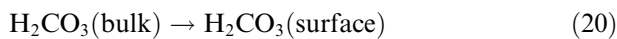
(3) Electrochemical reactions at the metal substrate surface

$$2H_2CO_3 + 2e^- \leftrightarrow H_2 + 2HCO_3^- \tag{23}$$
$$2HCO_3^- + 2e^- \leftrightarrow H_2 + 2CO_3^{2-} \tag{24}$$
$$2H^+ + 2e^- \leftrightarrow H_2 \tag{25}$$
$$Fe \leftrightarrow Fe^{2+} + 2e^- \tag{26}$$
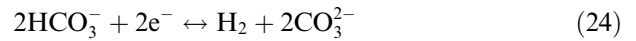
(4) Transportation of products from metal substrate surface to the bulk solution

$$Fe^{2+}(surface) \rightarrow Fe^{2+}(bulk) \tag{27}$$
$$CO_3^{2-}(surface) \rightarrow CO_3^{2-}(bulk) \tag{28}$$
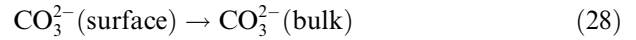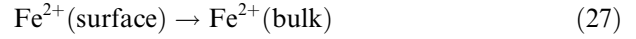
Assuming that the dominating electrochemical corrosion reaction is Eqs. (25) and (26), the diffusion coefficient D_{H^+} for H^+ and $D_{Fe^{2+}}$ for Fe^{2+} are, respectively, 9.31×10^{-9} m²/s and 7.12×10^{-10} m²/s.

2.2. Discretization and solution method

The fluids are assumed to be incompressible and isothermal and to have constant fluid properties. The finite volume method is used to discretize the transport equation. Many methods are used to improve the accuracy and convergence of the VOF solution. The second-order upwind differencing scheme is used for solving the momentum equation to minimize numerical diffusion and the first-order explicit time marching scheme is used for solving the unsteady formulation. The interface between gas and liquid are reconstructed using piecewise linear interface calculation (PLIC) proposed by Youngs [9]. To improve a rapid convergence rate without any significant loss of accuracy, the pressure-implicit with splitting of operators (PISO) pressure–velocity coupling scheme, which is based on the higher degree of the approximate relation between the corrections for pressure and velocity, is used for the pressure–velocity scheme. When large body forces exist in multiphase flows, the body force and pressure gradient terms in the momentum equation are almost in equilibrium, with the contributions of convective and viscous terms small comparatively. Segregated algorithms converge poorly unless partial equilibrium of pressure gradient and body forces is taken into account, and an optional implicit body force treatment that can account for this effect, making the solution more robust. The time step size sets as 10^{-4} s, maximal iterations per time step is 150, and the total simulation time is around 0.85 s, which is enough for a terminal constant falling liquid film thickness and velocity formation.

2.3. Model geometry and boundary conditions

A two-dimensional coordinates system assuming axial symmetry about the centerline of the pipe is used. The pipe diameter is 36 mm and the tube length is 500 mm. To ensure the results independent of grid, the computational results are validated by the experimental results for Taylor bubble rising velocity in stagnant liquid. The uniform grid
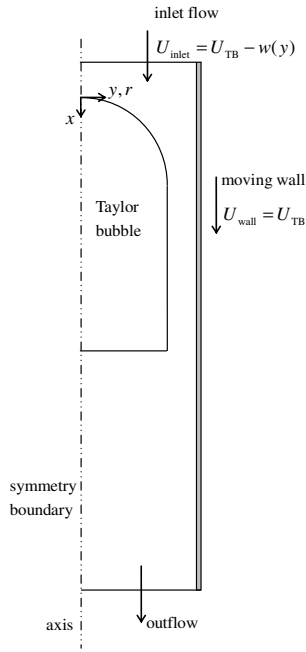
Fig. 1. Schematic map of a moving coordinates system attached to the Taylor bubble nose in a vertical pipe.

is initially used in the simulation process. It is found that the grid density with 42×500 uniform quadrilateral control volumes is high enough to gain the computational results in the radial and axial directions. To gain the effects of the falling liquid film on the near wall mass transfer and shear stress, the grid is firstly uniformly meshed with 42×500 quadrilateral control volumes, then the first-row grid next to the wall is uniformly refined by subdividing it into 5 control volumes along the radial direction. Thus, there are total 50×500 control volumes in the domain.

The initial shape of the bubble is assumed to be the combination of a cylindrical body and a hemispherical nose. The cylindrical body with a diameter of 32 mm and a height of 180 mm ($5D$), and the hemispherical nose with a radius of 16 mm with the center of the sphere on the end face center of the cylindrical body. The arbitrarily initial shaped Taylor bubble is simulated and finally a steady bubble shape is developed.

Fig. 1 shows the boundary conditions, and the no-slip condition is applied to the tube wall. With a reference frame attached on the rising Taylor bubble, the tube wall moves downward with velocities $U_{\text{wall}} = U_{\text{TB}}$, $V_{\text{wall}} = 0$, while the Taylor bubble becomes stationary. At the top computational domain boundary, the inlet flow boundary condition is imposed with a velocity profile $U_{\text{TB}} - w(y)$, $V = 0$, the fully developed velocity profile $w(y) = U_{\text{L}}$, and $w(y) = 0$ for the Taylor bubble rising in a stagnant liquid. At the bottom computational domain boundary, the outflow boundary condition is imposed with a parallel velocity profile and $\partial U/\partial x = 0$, $V = 0$. At the axis of symmetry, $\partial U/\partial y = 0$, $V = 0$. At the interface between liquid and gas with zero shear stress $(\bar{\tau} \cdot \tilde{\mathbf{n}}) \cdot \tilde{\mathbf{s}} = 0$, on the gas-phase

side of the interface, the pressure can be taken to be uniform constant pressure, $p = \text{constant}$, and the kinematic condition $\mathbf{u} \cdot \mathbf{n} = 0$. The initial U_{TB} is imposed with a guess value, which is then adjusted until the bubble is no longer drift up or down in the axial direction.

3. Results and discussion

The hydrodynamic characteristics of gas–liquid vertical upward slug flow are affected by many parameters such as viscous, interfacial, and inertial forces, physical properties of fluids, and geometrical topography [10–12]. According to the dimensionless analysis based on Pi-theorem, there is a set of dimensionless group as follows:

$$\sqrt{\frac{gD^3 \rho_{\text{L}}(\rho_{\text{L}} - \rho_{\text{G}})}{\mu_{\text{L}}^2}}, \frac{gD^2(\rho_{\text{L}} - \rho_{\text{G}})}{\sigma}, U_{\text{TB}} \bigg/ \sqrt{\frac{gD(\rho_{\text{L}} - \rho_{\text{G}})}{\rho_{\text{L}}}}, \frac{\mu_{\text{G}}}{\mu_{\text{L}}}, \frac{L_{\text{TB}}}{D}$$

Due to the density and viscosity of the gas much less than those of the liquid, $(\rho_{\text{L}} - \rho_{\text{G}})/\rho_{\text{L}}$ can be taken as unity, and $\mu_{\text{G}}/\mu_{\text{L}}$ is of neglected importance. For a fully developed gas–liquid two-phase upward slug flow, the translational propagating velocity is independent of the length of the Taylor bubble L_{TB}/D [13–17]. Therefore, three dimensionless numbers can sufficiently describe the hydrodynamic characteristics of upward slug flow, which are the inverse viscosity number $N_{\text{f}} = \rho_{\text{L}}(gD^3)^{0.5}/\mu_{\text{L}}$, the Eötvös number $Eo = \rho_{\text{L}} gD^2/\sigma$, and the Froude number for Taylor bubble $Fr_{\text{TB}} = U_{\text{TB}}/(gD)^{0.5}$.

The terminal velocity of the falling liquid film and the shape of the Taylor bubble, are significantly affected by the viscous, interfacial, and inertial forces [10–12]. White and Beardmore [10] investigated the velocity of a single cylindrical air bubble through liquids contained in vertical tubes, and found that the viscous effects are of minor importance if $N_{\text{f}} > 550$, interfacial effects if $Eo > 70$ and inertial effects if $Fr_{\text{TB}} < 0.05$. Fabre and Line [11] concluded that the viscous, interfacial and inertial forces have different influences on the Taylor bubble shape, the Taylor bubble nose edge shaped like prolate spheroidal and the Taylor bubble bottom edge shaped like oblate spheroidal, flat or concave.

Taylor bubble rising velocity is a very important parameter in upward gas–liquid slug flow, deeply investigated by Dumitrescu [13], Nicklin [16], etc. An empirical correlation for Taylor bubble rising velocity U_{TB} in a flowing liquid can be expressed as follows:

$$U_{\text{TB}} = C_1 U_{\text{m}} + U_{\text{TB0}} \tag{29}$$

Namely,

$$Fr_{\text{TB}} = C_1 Fr_{\text{m}} + Fr_{\text{TB0}} \tag{30}$$

where C_1 is a dimensionless coefficient dependent on the velocity profile ahead of the Taylor bubble, for turbulent flow, $C_1 = 1.2$, and for laminar flow, $C_1 = 2$ [16,18]; Fr_{m} the Froude number based on the mixture velocity U_{m}, the sum of the superficial liquid velocity U_{SL} and superficial

gas velocity U_{SG}; Fr_{TB0} is the Froude number for Taylor bubble drifting in stagnant liquid due to buoyancy of Taylor bubble, which is a function of N_f, Eo and inclination θ, namely Fr_{TB0} (N_f, Eo, θ) [13,14,16].

In this work, CFD simulations of hydrodynamic characteristics for gas–liquid vertical upward slug flow using VOF method have been performed with a variety of inverse viscosity number N_f, Eötvös number Eo, and Froude number of Taylor bubble Fr_{TB}. The ranges of N_f, Eo and Fr_{TB} are 10.1–2.1 × 10^4, 0–1.59 × 10^2 and 0–4.283, respectively.

3.1. Taylor bubble shape

3.1.1. Viscosity dominant

Fig. 2 shows the effect of N_f on the Taylor bubble shape with $Eo = 158$ in a stagnant liquid. In this case, $Eo > 70$, the effect of surface tension can be neglected according to the conclusion of White and Beardmore [10]. It can be seen that the Taylor bubble nose edge is shaped like prolate spheroidal, and the curvature decreases with increased N_f. The Taylor bubble bottom edge shape is changed from an oblate spheroid to a redented surface when N_f is increased from 9.01 × 10^1 to 4.26 × 10^2, then continuously changed

Fig. 2. Effects of different values of N_f on the Taylor bubble shape with $Eo = 158$ in a stagnant liquid: (a) $N_f = 9.01 \times 10^1$; (b) $N_f = 4.26 \times 10^2$; (c) $N_f = 2.1 \times 10^4$.

from a redented surface to a concave surface when N_f is further increased from 4.26 × 10^2 to 2.1 × 10^4. The calculated results of Taylor bubble shape are consistent with the experimental results of Goldsmith and Mason [19]: the flattening or concaving shape of Taylor bubble bottom edge when the flow is not the viscosity-dominated, and the oblate spheroid shape of Taylor bubble bottom edge when the flow is the viscosity-dominated regime. White and Beardmore [10] found that the critical criteria is $N_f = 550$, while Fabre and Line [11] stated that it is $N_f = 300$. Nevertheless, it is difficult to define the criteria for the case there is no distinct transformation boundary from oblate spheroid to concave surface. The results of CFD simulation show that the Taylor bubble bottom edge shape is a redented surface when the N_f is from 350 to 680. Fig. 2 also shows the streamlines of liquid phase in the Taylor bubble nose zone and in the Taylor bubble wake zone in a reference frame attached to the Taylor bubble. Away from the front of the Taylor bubble nose zone, the streamlines of liquid phase are very parallel. In the Taylor bubble nose zone, the streamlines of liquid phase are pushed aside to the tube wall, and small vortexes are formed around the stagnation point on the Taylor bubble tip. The size of vortex is significantly affected by the curvature radius of Taylor bubble nose, which decreases with the increase of curvature radius of Taylor bubble nose, resulting in the increase of N_f number, and even the vortex disappears when $N_f = 2.1 \times 10^4$.

In the Taylor bubble wake zone, primary vortexes in various sizes with vigorous mixing and strong circulation are formed when the annular falling liquid film flows over the Taylor bubble bottom and plunges into the wake. The liquid coming from the falling film smoothly expands after the bubble trailing edge, inducing the formation of a recirculation in the wake rising attached to the bubble. The velocity of the falling liquid film rapidly decays due to this mixing, which makes the film cease its continuous downward movement. The plunge process can be regarded as an annular liquid jet plunging into a stagnant liquid slug pool, generating a gravitational wave. Gravitational wave makes the liquid phase change directions from downward flow near the tube wall to upward flow near the tube axis, which further results in the formation of secondary vortexes near the tube wall immediately following the primary vortexes.

The hydrodynamic characteristic of Taylor bubble wake is of great importance to modeling slug flow, which plays a pivotal role for the interaction of consecutive Taylor bubbles. The viscosity has a significant effect on the streamlines in the Taylor bubble wake zone. As shown in Fig. 2, with the increased degree of oblateness, the scale and intensity of circulatory vortex are all decreased, and the streamlines are changed evenly. It is also found that the higher the viscosity, the less the distortion and the smaller the fluctuation of the Taylor bubble bottom, the fewer small bubbles are shed off from the Taylor bubble wake and entrained in the wake vortexes. In this case, the falling liquid film is
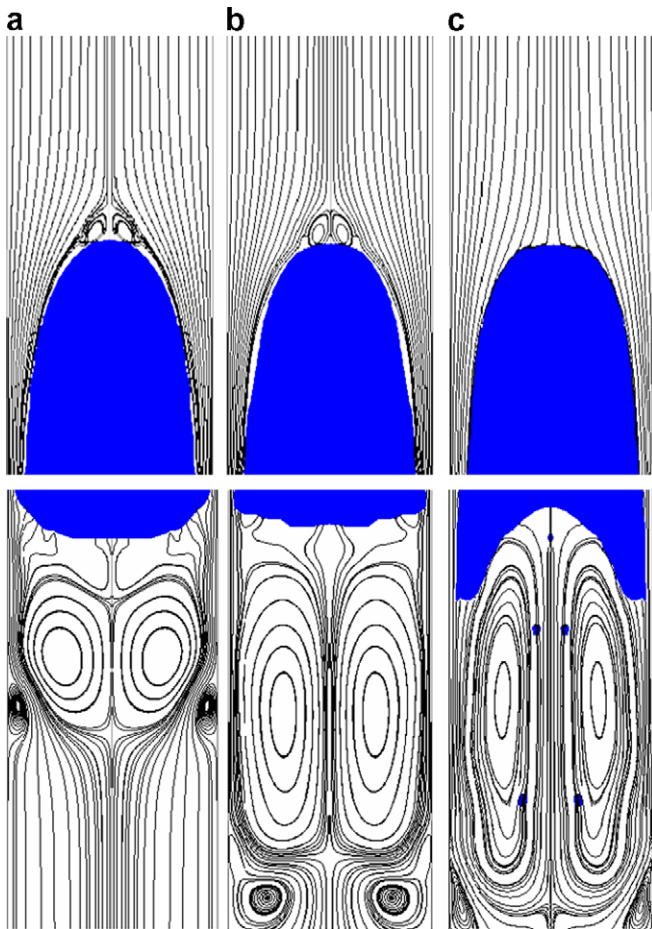
slowed down with the increased open area, and the different streams of liquid are rejoined together at some position downstream forming close vortexes. At higher N_f, small bubbles are shed off from the Taylor bubble wake, which have a great effect on the streams of liquid in the Taylor bubble wake zone. In this case, the streams are not rejoined together downstream, leading to an open wake with some vortexes shedding off. For the situations where $Eo > 680$, $Fr_{TB} = 0.351$, Campos and Guedes de Carvalho [20] found that a laminar flow-closed and axisymmetric wake with internal recirculatory flow for $N_f < 500$, transitory flow-closed unaxisymmetric wake with internal recirculatory flow for $500 < N_f < 1500$, and turbulent flow-open and perfectly mixed wake for $N_f > 1500$. The results of CFD simulations are consistent with the conclusion of the Campos and Guedes de Carvalho [20].

An important parameter that attention should be paid to is the minimum stable liquid slug length, namely the minimum distance for restoring a fully developed velocity distribution in the liquid slug. Aladjem Talvy [21] found that the succeeding Taylor bubble dose not affect the motion of the leading one and is sensitive to the velocity distortion in the wake of the leading elongated bubble. Therefore, it can be deduced that the minimum stable liquid slug length is intimately related to the penetration distance of falling liquid film from the Taylor bubble bottom edge to the secondary vortexes. The secondary vortexes have the opposite sense of rotation compared to the primarily vortexes. When the length of liquid slug is less than penetration distance, the falling liquid film holds an annular space, leading to an increase of upward velocity of liquid, the succeeding Taylor bubble rising velocity as well. However, the penetration distance of the falling liquid film has no effect on the succeeding Taylor bubble when the liquid slug is greater than the penetration distance. The penetration distance of falling liquid film is dependent on the terminal velocity and the thickness of fully developed falling liquid film.
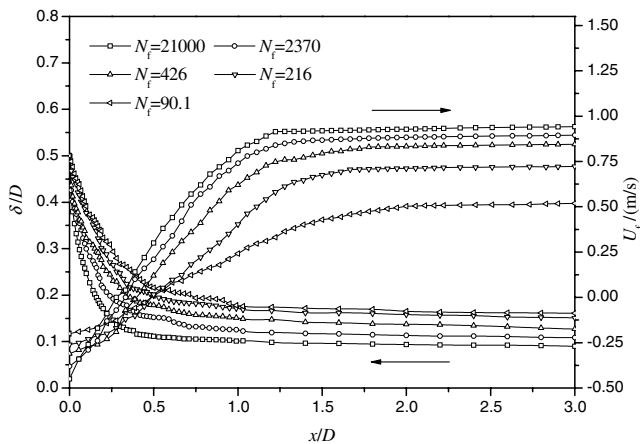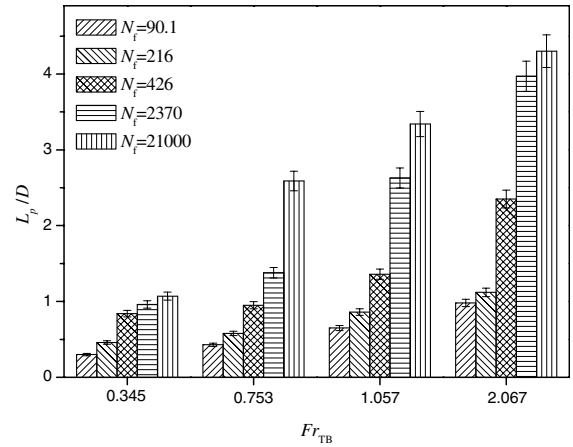
Fig. 4. Penetration distances of falling liquid film at different values of N_f and Fr_{TB} with $Eo = 158$.

Fig. 3 shows the velocities and normalized thicknesses of falling liquid film along the Taylor bubble length at different values of N_f. The dimensionless thickness of falling liquid film (δ/D) decreases with increased the dimensionless distance to the nose (x/D), until it reaches a constant thickness at a certain distance from the nose. The thickness of falling liquid film is decreased with increased N_f, whereas the velocity of falling liquid film changes contrarily. At low N_f due to the higher viscosity, the shear stress in the liquid is high. The stress induced by momentum diffusion slows down the fluid coming from the liquid film, making the liquid film expansion take place closer to the bubble bottom, thereby the penetration distance of falling liquid film decreases. As shown in Fig. 4, the penetration distance L_p of the falling liquid film is increased with increased N_f, namely the increase of the minimum stable liquid slug length.

3.1.2. Surface tension dominant

Fig. 5 shows the effect of Eo on the Taylor bubble shape with $N_f = 18,500$ in a stagnant liquid. Due to $N_f > 550$, the viscous effect can be neglected [10,11]. The degree of prolateness of the Taylor bubble nose edge is increased with decreased Eo. Similar to the effect of N_f on the shape of Taylor bubble bottom edge, the Taylor bubble bottom edge is changed from a concave surface to a redented surface when Eo is decreased from 160.2 to 63.5, and further changed oblateness from a redented surface to an oblate surface when Eo is continuously decreased from 63.5 to 4.23. The curvature of the Taylor bubble nose edge is increased with increased surface tension, resulting in the increase of the thickness of falling liquid film. The increased curvature gives rise to an increase of the size of the vortex, which are formed around the stagnation point on the Taylor bubble tip. The increase of the thickness of falling liquid film makes the increase of the distance from the formation of the fully developed falling liquid film to the Taylor bubble nose, and the decrease of the velocity of fully developed falling liquid film. In the Taylor bubble
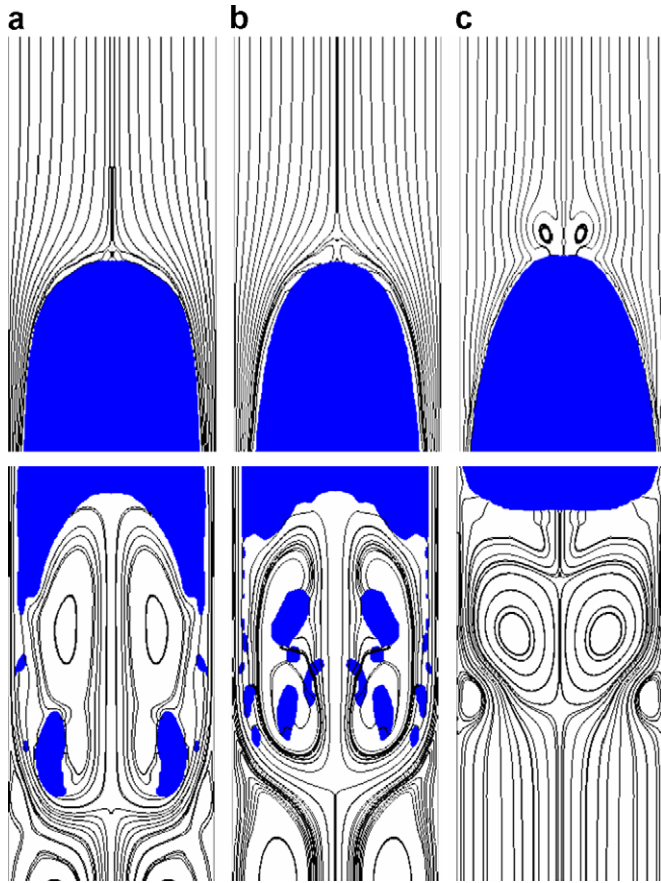
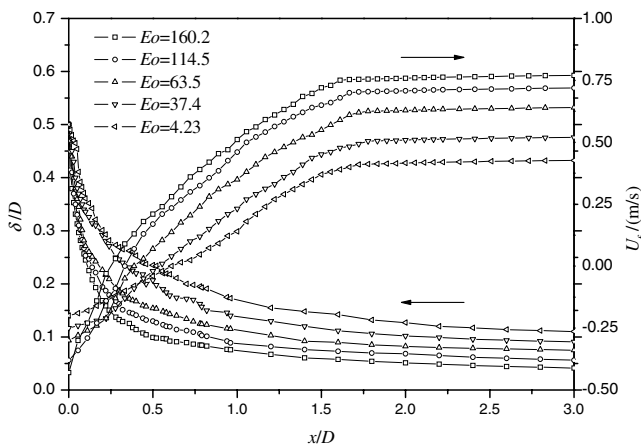

Fig. 3. Velocities and normalized thicknesses of falling liquid film along the Taylor bubble length at different values of N_f with $Eo = 158$ in a stagnant liquid.
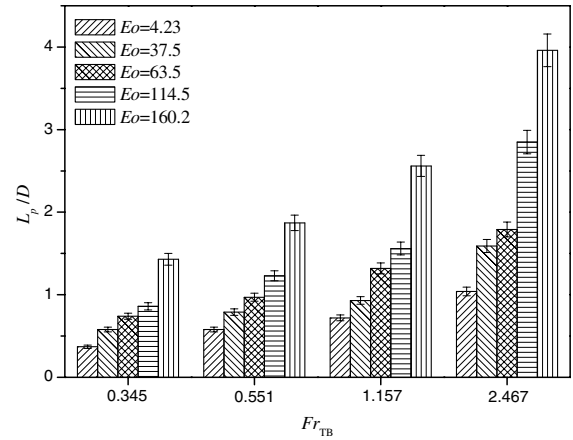
Fig. 5. Effects of different values of *Eo* on the Taylor bubble shape with $N_f = 18,500$ in a stagnant liquid: (a) $Eo = 160.2$; (b) $Eo = 63.5$; (c) $Eo = 4.23$.

Fig. 7. Penetration distances of falling liquid film at different values of *Eo* and Fr_{TB} with $N_f = 18,500$.

wake zone, from the results of CFD simulation it is found that there is the same effect tendency of the surface tension on the streamlines in the Taylor bubble wake zone as that of viscosity, the higher the surface tension, the less the distortion and the smaller the fluctuation of the Taylor bubble

Fig. 6. Velocities and normalized thicknesses of falling liquid film along the Taylor bubble length at different values of *Eo* with $N_f = 18,500$ in a stagnant liquid.

bottom, the fewer small bubbles are shed off from the Taylor bubble wake and entrained into the wake vortexes.

Fig. 6 shows the velocities and normalized thicknesses of falling liquid film along the Taylor bubble length at different values of *Eo*. Fig. 7 shows the penetration distance of falling liquid film at different values of *Eo*.

3.1.3. Inertia dominant

When the effects of N_f and *Eo* on the Taylor bubble shape are of less importance than those of Fr_{TB}, the hydrodynamic characteristics of slug flow can be regarded as the Taylor bubble rises in a tube containing a perfect fluid without viscosity or surface tension, namely the flows are dominated by inertia. As a matter of fact, most of the practical cases of slug flow will fall within the frame of the inertia-dominant regime. In the inertia-dominated regime, the viscosity and surface tension can be neglected if $N_f > 550$, $Eo > 70$ according to White and Beardmore [10], or $N_f > 300$, $Eo > 100$ according to Wallis [22].

Fig. 8 shows the effect of Fr_{TB} on the Taylor bubble shape with $N_f = 2.1 \times 10^4$ and $Eo = 134$. Due to $N_f > 550$ and $Eo > 70$, the effects of viscosity and surface tension can be neglected [10], and the flow can be regarded as inertia-dominated flow. The Taylor bubble nose edge is shaped like prolate spheroidal, and the value of Fr_{TB} has a weak effect on the Taylor bubble nose shape, whereas the Taylor bubble bottom edge shape is changed from flattening to concaving with increased Fr_{TB}. When the degree of concaving is high, the Taylor bubble bottom is easily distorted and the Taylor bubble bottom edge has a large oscillation, which will induce to shed off many small bubbles from the Taylor bubble bottom. Fig. 8 also shows the streamlines of liquid phase in the Taylor bubble nose zone and in the Taylor bubble wake zone in a reference frame attached to the Taylor bubble. In the Taylor bubble nose zone, the streamlines are of concordance at the different values of Fr_{TB}. The number of the small bubbles shedding off from the Taylor bubble bottom is increased with increased Fr_{TB}.
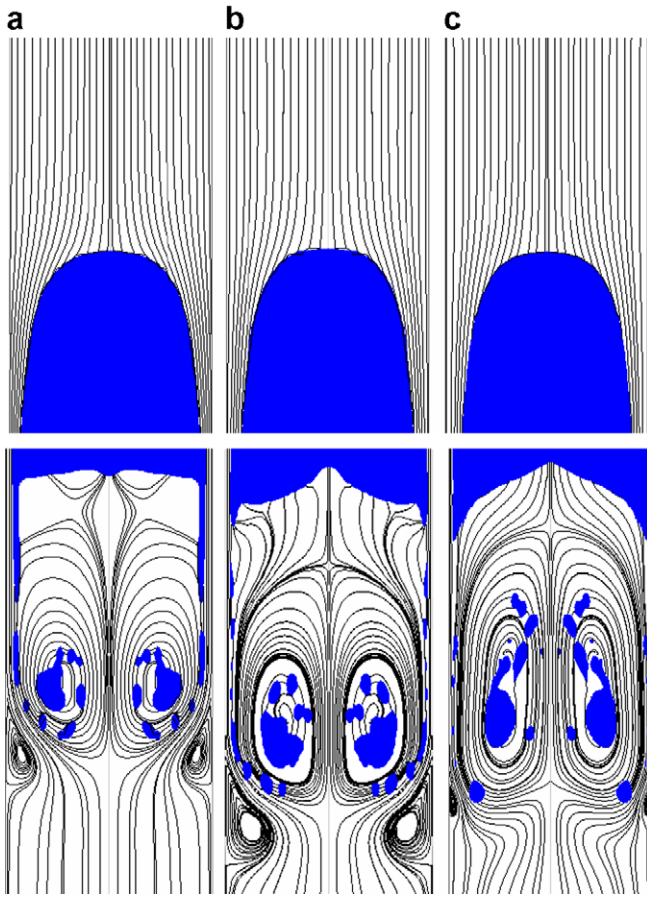
Fig. 8. Effects of different values of Fr_{TB} on the Taylor bubble shape with $N_f = 2.1 \times 10^4$ and $Eo = 134$: (a) $Fr_{TB} = 1.057$; (b) $Fr_{TB} = 2.067$; (c) $Fr_{TB} = 3.283$.

In a stagnant liquid, provided that the viscosity and surface tension effects can be neglected, the annular falling liquid film around the Taylor bubble nose can be assumed to be a liquid film without interfacial shear. Therefore, the hydrodynamic characteristics of falling liquid film in the Taylor bubble nose zone obey the potential flow theory, and the Taylor bubble nose is a spherical cap [13,14]. In a flowing liquid, the characteristics in the Taylor bubble nose zone can also be explained by potential flow theory [16]. A universal expression for the Taylor bubble nose curvature radius, $r = 0.75R$, was proposed by Brown [15] and Collins [18]. According to Bugg [23,24], Fabre and Line [11], inertial force dominates at $Mo = 2.1 \times 10^4$, $Eo = 134$, the Taylor bubble bottom should be flat and slightly concave downward with small bubbles breaking away at the outer edges and reentering in the center. The Taylor bubble nose shape is observed to be like a spherical cap and independent of the bubble length, whereas there is a more or less deviation from spherical cap for most practical bubbles. The predicted Taylor bubble shape by the VOF model matches reasonably well with that observed by previous experiments, validating the model to be correct qualitatively.

The elongated Taylor bubble can be divided into three parts according to the configuration profile. The first part is prolate spherical cap zone, the third part is the terminal cylinder zone with terminal constant thickness and velocity of fully developed falling liquid film, and the second part is the transition zone between the prolate spherical cap and the terminal cylinder. For situations where inertia dominates the flow, Dumitrescu [13] and Davis and Taylor [14] found that the first part can be regarded as a spherical cap and the annular developing falling liquid film is formed around the first part. According to pure potential flow theory and Bernoulli formula, the annular developing falling liquid film thins as it flows over the first part and the second part with a velocity $(2gx)^{0.5}$ relative to the bubble at a distance x from the Taylor bubble nose until the terminal constant velocity and thickness of the fully developed falling liquid film are achieved. In the third part, the gravitational force of the film balances the resultant force of wall friction force and interfacial force. The viscosity and surface tension cannot be neglected and the potential flow theory is inappropriate to the fully developed falling liquid film zone. On the contrary, in the Taylor bubble nose zone, namely in the first part and in the second part, which is inertia controlled and the liquid surface tension and viscosity can be neglected. As a result, the flow characteristics of falling liquid film in the Taylor bubble nose zone obey the potential flow theory.

Dumitrscu [13] found that the Taylor bubble nose can be regarded as a spherical cap with a radius that is $3D/8$, and suggested a formula for the curvature radius of spherical bubble cap, r_1, as follows:

$$r_1 = \frac{1}{2}\sqrt{x(3D - 4x)} \tag{31}$$

Davies and Taylor [14] suggested a relationship for the curvature radius of the second part of the Taylor bubble, r_2, as follows

$$r_2 = \frac{D}{2}\sqrt{1 - \frac{U_0}{\sqrt{2gx}}} \tag{32}$$

where U_0 is the Taylor bubble drift velocity in stagnant liquid, g is the gravitational acceleration. In the inertia-dominated flow, $U_0 = 0.35(gD)^{0.5}$. Nevertheless in the third region, namely in the fully developed falling liquid film zone, the film thickness depends on physical properties of fluids.

Fig. 9 shows the velocities and normalized thickness of falling liquid film along the Taylor bubble length at different Fr_{TB}. The variation of this normalized thickness represents the Taylor bubble shape. It can be seen that the curvature radius of Taylor bubble nose changes little with Fr_{TB}, which further verifies that the Taylor bubble is insensitive to the superficial velocities and the bubble length, and the results are consistent with Dumitrescu's [13], Davis and Taylor's [14] and Brown's [15] results. The Taylor bubble nose curvature radius is $r = 0.73R$, smaller than Brown's results, which may be caused by the difference of CFD simulation conditions and experimental conditions.
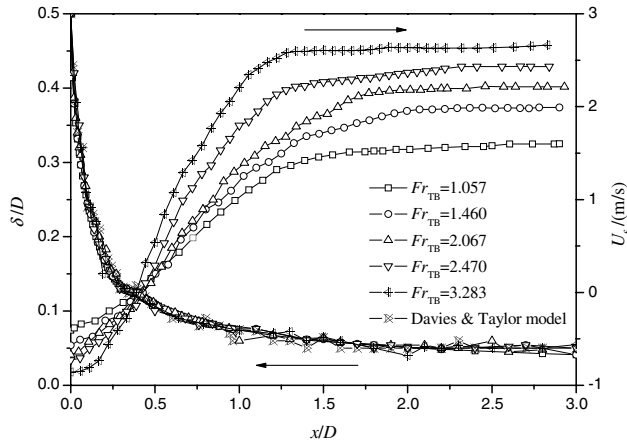
Fig. 9. Velocities and normalized thicknesses of falling liquid film along the Taylor bubble length at different values of Fr_{TB} at $N_f = 2.1 \times 10^4$ and $Eo = 134$.

Fig. 10. Penetration distances of falling liquid film at different values of Fr_{TB} with $N_f = 2.1 \times 10^4$ and $Eo = 134$.

Nevertheless, it is found that the normalized thickness of falling liquid film cannot be elucidated by the potential flow theory when the flows are dominated by viscosity or surface tension, as shown in Figs. 3 and 6.

The parameters associated with the falling liquid film become crucial for modeling slug flow induced corrosion. For instance, the vortex intensity in the liquid slug may be closely related to the falling liquid film velocity in the bottom of the Taylor bubble, which is the function of the film thickness. If the downward velocity is designated to be positive, the axial velocity component profile of the falling liquid film along the Taylor bubble length at different Fr_{TB} is shown in Fig. 9. Due to buoyancy, the Taylor bubble moves upward faster than the liquid, and the liquid in front of its nose is pushed moving upward with a negative velocity. At about the length of $0.5D$ from the Taylor bubble nose, the developing falling liquid film is formed, and continuously accelerated with a positive velocity until the fully developed falling liquid film is reached at about the length of $1.5D$–$2.1D$ from the Taylor bubble nose. Though the curvature radius of Taylor bubble nose changes little with increased Fr_{TB}, the velocity of fully developed falling liquid film is increased with increased Fr_{TB}, as shown in Fig. 9.

The effect of Fr_{TB} on the penetration distance of falling liquid film can be seen in Fig. 10. Similar to Figs. 4 and 7, it can be seen that the increased Fr_{TB} will always increase the penetration distance of falling liquid film.

3.2. Taylor bubble rising velocity in stagnant liquid

According to Eq. (30), the Taylor bubble rising velocity in a flowing liquid is closely related to Taylor bubble rising velocity in a stagnant liquid, namely Fr_{TB} is related to Fr_{TB0}. In vertical upward flow, when the viscosity and surface tension can be neglected, Fr_{TB0} is a constant value, 0.351 by theory and 0.346 by experiments of Dumitrescu [13], 0.328 determined by Davies and Taylor [14], and
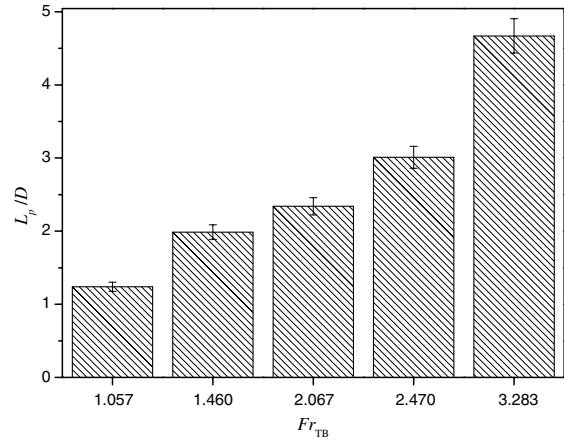
0.345 obtained by experiments of White and Beardmore [10]. When the flows are dominated by surface tension, the hydrostatic force may be balanced by surface tension. Surface tension can monotonically reduce the Taylor bubble rising velocity. When $Eo < 3.37$ the bubbles cannot move with zero rising velocity. Bendiksen [25] found the effect of Eo on the Fr_{TB0} as follows:

$$Fr_{TB0}(N_f \to \infty, Eo, 90°)$$
$$= 0.344 \frac{1 - 0.96e^{-0.0165Eo}}{(1 - 0.52e^{-0.0165Eo})^{3/2}} \sqrt{1 + \frac{20}{Eo}\left(1 - \frac{6.8}{Eo}\right)} \quad (33)$$

When the flows are dominated by viscosity, Wallis [22] proposed a correlation as follows:

$$Fr_{TB0}(N_f, Eo \to \infty, 90°) = 0.345(1 - e^{-0.01N_f}) \quad (34)$$

Wallis [22] proposed a general correlation for Taylor bubble rising velocity in terms of relevant variables of N_f and Eo as follows:

$$Fr_{TB0} = 0.345(1 - e^{-\frac{0.01N_f}{0.345}})(1 - e^{\frac{3.37-Eo}{m}}) \quad (35)$$

where $N_f > 250$, $m = 10$; $18 < N_f < 250$, $m = 69/(N_f)^{0.35}$; $N_f < 18$, $m = 25$.

Fig. 11 shows the calculated results by CFD simulation for Taylor bubble rising velocity Fr_{TB0} plotted as a function of Eo and Mo in stagnant liquids, where Mo is Morton number, $Mo = Eo^3/N_f^4 = g(\mu_L)^4/(\rho_L\sigma^3)$. It can be seen that the results agree well with a wide range of experimental results of White and Beardmore [10], and the maximum deviation is within $\pm10\%$. Fr_{TB0} is increased with decreased Mo at a constant Eo, and Fr_{TB0} approaches 0.345 when $Eo > 70$ and $Mo < 10^{-2}$ for situations where flows are dominated by inertia. The flow is dominated by surface tension when $Eo < 70$ and $Mo < 3.8 \times 10^{-6}$, whereas the flow is dominated by viscosity when $Eo > 70$ and $Mo > 3.8 \times 10^{-6}$. When $Fr_{TB0} < 0.05$, the Taylor bubble
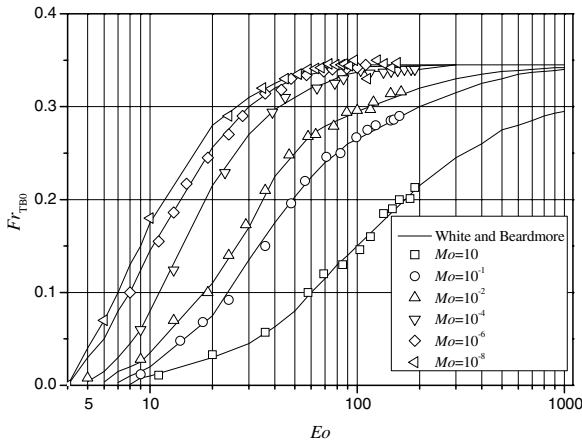
Fig. 11. Taylor bubble rising velocities in stagnant liquids in vertical tube.

rising velocity is so small that the bubble can be regarded still in liquid and the inertia is of neglected importance.

3.3. Velocity fields

Most of the practical slug flows are inertia-dominated. Thereby the analyses on velocity field are focused on these situations. Fig. 12 shows the velocity filed of slug flow with $Fr_{TB} = 0.47$, $N_f = 2.1 \times 10^4$ and $Eo = 147$ in a reference frame attached on the Taylor bubble (left) and in an inertial reference frame (right). The left side of the axis of symmetry shows velocity vectors while the right side shows the streamlines.

The velocity field obtained in the Taylor bubble nose zone is shown in Fig. 12a,a′. In a fixed reference frame, it can be easily observed that the Taylor bubble moves upwards. There is no noticeable radial velocity along the tube axis far away ahead of the bubble, and the axial velocity drops off quite rapidly ahead of the bubble, decreases to about 15% of the Taylor bubble rising velocity at about $0.5D$ ahead of the Taylor bubble nose tip, as shown in Fig. 13. Near the Taylor bubble nose tip, the liquid in front of the bubble is pushed forward and away from the centre and starts to fall around the bubble, forming a thin liquid film. The velocity field near the region of the bubble nose tip and away from the tube axis is characterized by a significant radial velocity, making the liquid move into the falling liquid film and start flow downwards.

If the axial downward velocity component is designated to be positive, and radial velocity away from the tube axis is designated to be positive. A detailed quantitative axial and radial velocities at $x/D = 0$, -0.3 and -0.5 are shown in Fig. 13. At $r/R = 0$, the axial absolute value of negative velocity is maximum and the radial velocity is zero. The axial absolute value of negative velocity is decreased to zero when the r/R is increased from 0 to 0.5, and the axial absolute value of positive velocity is increased to maximum when the r/R is increased from 0.5 to 0.8, further the positive velocity is decreased to zero at $r/R = 1$. The radial
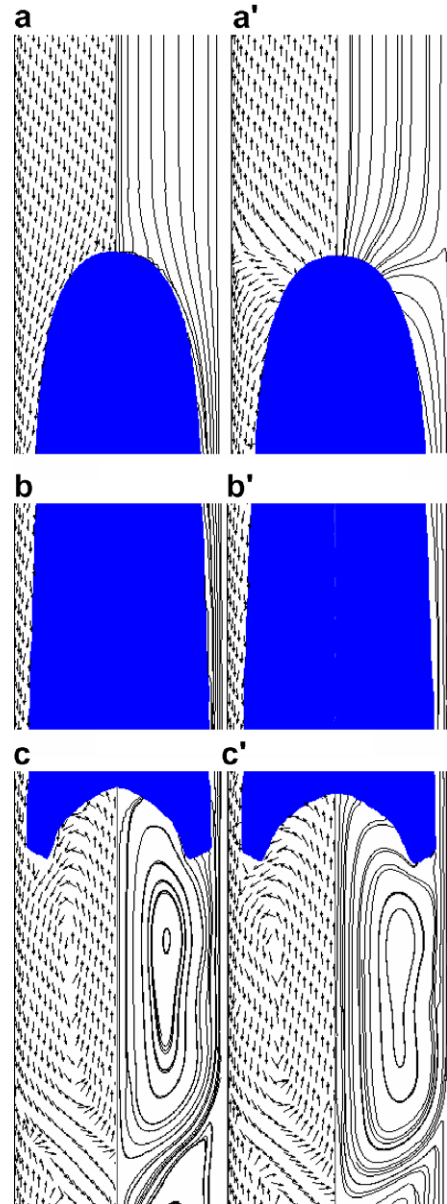

Fig. 12. Velocity fields of slug flow with $Fr_{TB} = 0.47$, $N_f = 2.1 \times 10^4$ and $Eo = 147$ in a reference frame attached on the Taylor bubble (left) and in a fixed reference frame (right), the left side of the axis of symmetry shows velocity vectors while the right side shows the streamlines.

velocity is increased to maximum when the r/R is increased from 0 to 0.47, then decreased to zero at $r/R = 1$.

Fig. 12b,b′ shows the liquid flowing around the bubble nose forms a falling liquid film between the gas–liquid interface and the pipe wall. As shown in Fig. 14, immediately below the Taylor bubble nose tip, the falling liquid film is not fully developed and the axial velocity in the film is not a function of radial position but of axial position. The liquid film is accelerated along the bubble as its thickness diminishes. The maximum axial velocity in the developing film is in the midway of wall and gas–liquid interface, while the maximum radial velocity is near the gas–liquid interface. Nevertheless, the radial velocity reduces
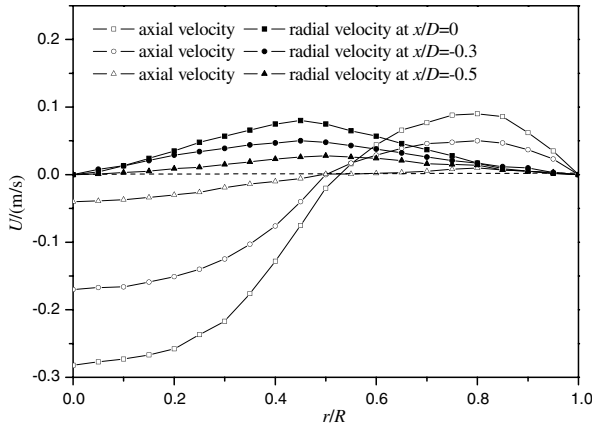
Fig. 13. Axial and radial components of velocity at $Fr_{TB} = 0.47$ (x is the distance from the Taylor bubble nose tip, the direction is positive along the Taylor bubble).

Fig. 15. Axial and radial velocity components of for Taylor bubble wake zone at $x/D = 0.5$, 1.0, 1.5 and 2.0 (x is the distance to the center of the Taylor bubble bottom edge) with $Fr_{TB} = 0.47$.

significantly to zero and the maximum axial velocity moves toward the gas–liquid interface with a constant value when the fully developed falling liquid film is achieved. The axial and radial velocities are changed little at $x/D = 3.0$ and 4.0, with the axial component higher than that at $x/D = 0.5$ and 1.5, and radial component lower than that at $x/D = 0.5$ and 1.5. This means at $x/D = 0.5$ and 1.5 the falling liquid film is not developed, while at $x/D = 3.0$ and 4.0 the falling liquid film is fully developed. It is also found that the gas–liquid interface location is $r/R = 0.73$ at $x/D = 3.0$ and 4.0, smaller than Brown's results [15].

The velocity field obtained in Taylor bubble wake zone is shown in Fig. 12c,c′. The Taylor bubble wake is the region where the main difference appears in the flow pattern affected by Fr_{TB}, the higher Fr_{TB}, the higher the annular falling liquid film jet velocity. A large recirculation zone is apparent in the wake of the bubble which is driven by the relatively high velocity film jet penetrating into the region below the bubble. The falling liquid film expands immediately at the end of the liquid film, following the Taylor bubble bottom edge shape and occupying the place left by the
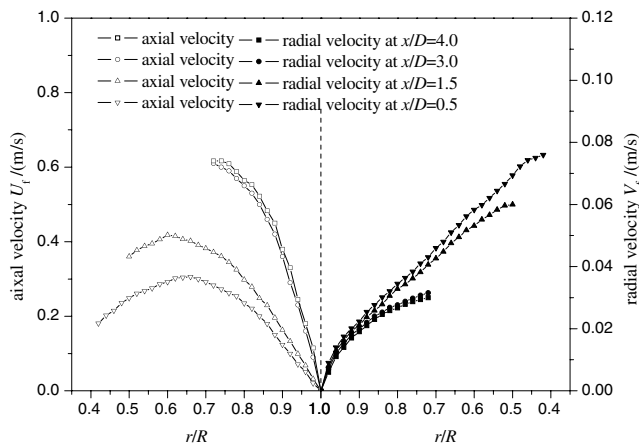

Fig. 14. Axial and radial components of velocity for falling liquid film at $x/D = 0.5$, 1.5, 3.0, and 4.0 with $Fr_{TB} = 0.47$.
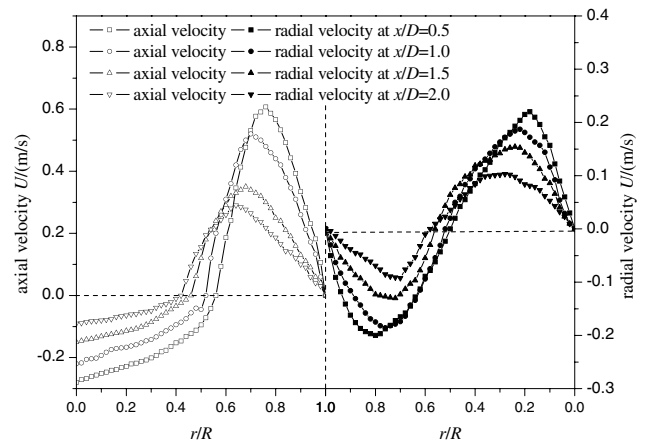
bubble during its ascending movement. The recirculation and the liquid film expansion are clearly seen, and the liquid changes direction and reattaches to the recirculation immediately below the wake zone. The turbulence made by liquid film plunging into the wake is the one of the causes for the instability of Taylor bubble bottom edge. The axial and radial velocity components in Taylor bubble wake zone vary considerably with the distance x/D from the bubble bottom as shown in Fig. 15. At the entrance to the Taylor bubble wake, the axial velocity is upward with the same velocity of Taylor bubble immediately below the whole bubble cross-section. Near the wall, the velocity changes direction and the profile attains a shape typical for a downward falling annular jet. This annular jet is quickly absorbed by the bulk liquid in the wake as the whole jet area widens. Fig. 15 shows the maximum negative axial velocity component at $r/R = 0$, $x/D = 0.5$ is larger than that at $r/R = 0$, $x/D = 1.0$ and 1.5, namely the axial velocity component decreases at the centerline of pipe with increased distance x from the Taylor bubble bottom. The maximum positive axial velocity components are decreased, and whose locations are decreased from $r/R = 0.82$ to 0.73 to 0.68 with increased x/D from 0.5 to 1.0 and 1.5. The maximum radial velocity components are also decreased with increased x/D, and the locations r/R as well. This means that the axial velocity component of falling liquid film is decelerated with increased x/D, and the recirculation occurs in the Taylor bubble wake zone.

3.4. Wall shear stress and mass transfer

Fig. 16 shows the wall shear stress along the Taylor bubble length at different Fr_{TB}. The wall shear stress is increased along the Taylor bubble length until the fully developed falling liquid film is attained, and it is also increased with increased Fr_{TB}. Nevertheless, the wall shear stress has a large fluctuation due to the chaotic and
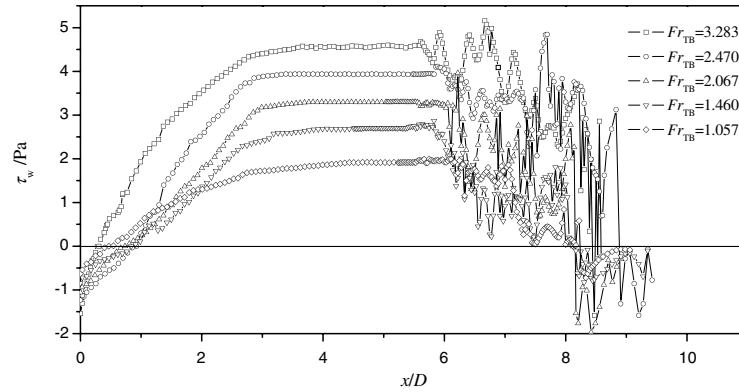
Fig. 16. Wall shear stresses along the Taylor bubble length at different Fr_{TB} with $N_f = 2.1 \times 10^4$ and $Eo = 147$.

turbulent vortexes in the Taylor bubble wake zone. The simulation results have a good agreement with the experimental results of Mao [26,27] and Nakoryakov [28].

Fig. 17 shows the average H^+ and Fe^{2+} mass transfer coefficients in both falling liquid film zone and Taylor bubble wake zone at different Fr_{TB}, respectively. It can be seen that the average mass transfer coefficient in the falling liquid film is always higher than that in the Taylor bubble wake zone. The Fe^{2+} mass transfer coefficient k_{Fe2+} is higher than that of H^+, as a result of largely different values of diffusion coefficient for H^+ and Fe^{2+}.

3.5. Slug flow induced CO_2 corrosion

Slug flow induced CO_2 corrosion is a complex phenomenon in which several simultaneous and interacting processes occur, inclusive of electrochemical reactions, mass transfer processes, and physical properties of corrosion product scale, metallurgical characteristics and hydrodynamics of slug flow. An effective mechanistic model incorporating seamlessly all of these factors is not available currently. CO_2 dissolves in water to give H_2CO_3, a weak

acid having a buffer for pH compared to mineral acids since it does not fully dissociated. There are two mass transfer gradients: one is that H^+ diffuses toward the metal substrate surface where pH increases, which is the function of H_2CO_3, HCO_3^-, and CO_3^{2-} concentrations; the other is the Fe^{2+} diffuses away from the metal substrate surface.

The H^+ mass transfer is the main culprit when the dominating electrochemical corrosion reactions are Eqs. (25) and (26) and the corrosion reaction rate-determining step is diffusion-controlled on the naked metal substrate. In this case, there are no corrosion rate limitations from electrochemical reaction effects and thus it could be seen as a worst case scenario. Assuming that all the hydrogen ions come from the dissociation of H_2CO_3, and that the pH is dependent on CO_2 partial pressure P_{CO_2} and temperature T, Fig. 18 shows the corrosion rates CR with different P_{CO_2} and Fr_{TB} based on the H^+ mass transfer coefficients as shown in Fig. 17. It can be seen that the corrosion rate is increased with increased Fr_{TB} and P_{CO_2}.

The Fe^{2+} mass transfer has a great influence on the formation of the corrosion product scale on the metal substrate surface. The corrosion product scale will not only establish the diffusion barrier between the metal substrate
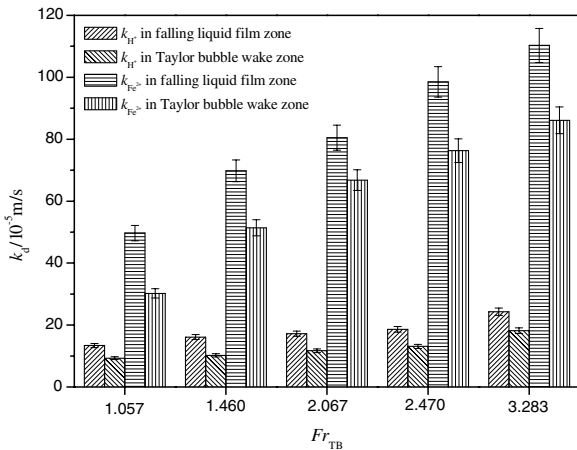

Fig. 17. Mass transfer coefficients of H^+ and Fe^{2+} in falling liquid film zone and Taylor bubble wake zone at different Fr_{TB} with $N_f = 2.1 \times 10^4$ and $Eo = 147$.
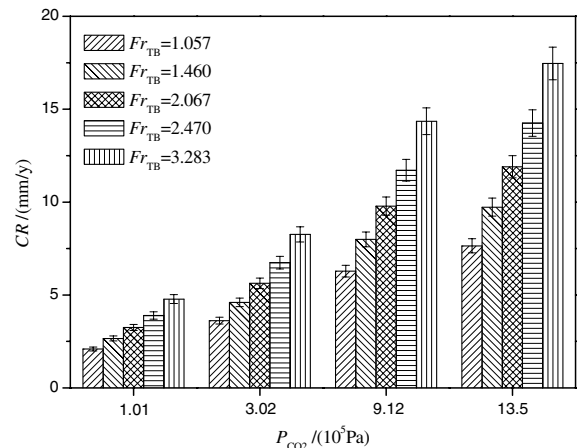

Fig. 18. Corrosion rates based on corrosion rate controlled by diffusion with different P_{CO_2} and Fr_{TB} at 65 °C.

and the corrosive medium, but also create a concentration gradient of the electrochemical reactant. The main corrosion product found in CO_2 corrosion in oil and gas pipelines is $FeCO_3$

$$Fe^{2+} + CO_3^{2-} \rightarrow FeCO_3 \qquad (36)$$

In the gas–liquid two-phase vertical upward slug flow induced CO_2 corrosion process, much attention has been paid to the formation of corrosion product scale. The precipitation and the morphology of the corrosion product scale depend on where and under what condition the precipitation occurs. According to the molecular theory, if super-saturation concentrations of Fe^{2+} and CO_3^{2-} next to the metal substrate surface are reached, by the van der Waals force the $FeCO_3$ particles can be attracted to the metal substrate surface, and then these particles may attract each other and eventually form a corrosion product scale. On the other hand, if the unsaturated Fe^{2+} and CO_3^{2-} are next to the metal substrate surface, these particles would be carried into the bulk solution due to the Brownian motion, and no corrosion product scale would occur. From a macroscopic view, the formation mechanism of corrosion product scale is much distinct. When the metal substrate surface is exposed to the corrosive environment, the ferrite corrodes away, leaving behind the pearlite platelets. Pearlite platelets can be regarded as a skeleton of the metal that remains after the rest of metal corroding away. When the flow of fluid is perpendicular to the pearlite platelets, these pearlites may create some stagnant conditions to anchor the $FeCO_3$ crystals to the surface, making a higher local concentrations of Fe^{2+} and CO_3^{2-}, which allow the crystals to grow larger and then the corrosion product scale is eventually formed. The formation of the compact and low-porosity will lower the exposed surface and hence reduce the uniform corrosion rate. Nevertheless, the localized corrosion rate will be very high if the corrosion product scale is not fully covered the entire metal substrate.

In the gas–liquid two-phase vertical upward slug flow induced CO_2 corrosion, the corrosion product scale is very brittle and easily broken up. If the hydrodynamic force is able to directly damage the corrosion product scale, the force must be high enough to overcome binding force in the crystal agglomerates of the scale and the adhesion force between the metal substrate and the scale. Previous investigations [29,30] found that the adherence of corrosion product scale to the metal substrate ranges from 10^6 to 3×10^7 Pa, fracture stress of high porosity corrosion product scale and low porosity corrosion product scale ranges respectively from 10^7 to 10^8 Pa and from 10^8 to 10^9 Pa, which are greatly larger than the hydrodynamic wall shear stress shown in Fig. 16. Therefore, the wall shear stress of upward gas–liquid slug flow is unable to directly damage the corrosion product scale.

However, when the corrosion product scale is uniformly deposited on the metal substrate surface, it will be more or less porous, leaving partial area of naked metal substrate directly exposed to the corrosive environment. The metal exposed to the corrosive environment corrodes away, resulting in many pits which grow underneath the neighboring $FeCO_3$ crystals and weaken their base. The hydrodynamic forces may further debond or break the binding force in the crystal agglomerates of the scale and the adhesion force between the metal substrate and the scale. Finally, the $FeCO_3$ crystals go into the main flow stream by a convection-mass-transfer mechanism. It can be seen that the wall shear stress of upward gas–liquid slug flow is alternate with high frequency, which is the key factor resulting in the corrosion product scale fatigue cracking.

4. Conclusions

Detailed CFD simulations of hydrodynamic characteristics of fully developed gas–liquid vertical upward slug flow and the mechanism of slug flow induced CO_2 corrosion have been carried out using the volume-of-fluid (VOF) method and following conclusions can be drawn:

1. CFD simulations demonstrate that the Taylor bubble nose edge shape is prolate spheroidal and the Taylor bubble bottom edge shape is oblate spheroidal, flat or concave. The hydrodynamic characteristics of slug flow are dominated by viscosity, surface tension and inertia force, which can be represented by dimensionless number N_f, Eo and Fr_{TB}. The curvature of the Taylor bubble nose edge is decreased with increased N_f or Eo when the flows are dominated by N_f ($N_f < 550$) or Eo ($Eo < 70$), whereas the curvature of Taylor bubble nose edge changes little with increased Fr_{TB}. The Taylor bubble bottom edge shape is changed from oblating to flattening, even concaving with the increased N_f, Eo, and Fr_{TB}.
2. When the flows are dominated by inertia, the velocity of fully developed falling liquid film is increased with increased Fr_{TB}. The developing falling liquid film is formed at about the length of $0.5D$ from the Taylor bubble nose, whereas the fully developed falling liquid film is reached at about the length of $1.5D$–$2.1D$ from the Taylor bubble nose. The CFD simulation results by the VOF model matches reasonably well with that observed by previous experiments, validating the model qualitatively correct.
3. CFD simulations show that the average mass transfer coefficient in the falling liquid film is always higher than that in the Taylor bubble wake zone. The iron ion near wall mass transfer coefficient is higher than that of hydrogen ion. The wall shear stress is increased with increased Fr_{TB} for fully developed falling liquid film, and the wall shear stress has a large fluctuation in the Taylor bubble wake zone. The formation and the damage mechanism of the corrosion product scale are proposed for the gas–liquid two-phase vertical upward slug flow induced CO_2 corrosion. It is found that the wall shear stress of upward gas–liquid slug flow is

alternate with high frequency, which is the key factor resulting in the corrosion product scale fatigue cracking.

Acknowledgement

References

[1] K.D. Efird, Flow-induced corrosion, in: R. Winston Revie (Ed.), Uhlig's Corrosion Handbook, 2nd ed., John Wiley & Sons Inc., New York, 2000, pp. 233–248.

[2] R. DeBar, Fundamentals of the KRAKEN code, Technical Report UCIR-760, LLNL, 1974.

[3] C.W. Hirt, B.D. Nichols, Volume of fluid (VOF) method for the dynamics of free boundaries, J. Computat. Phys. 39 (1981) 201–225.

[4] W.F. Noh, P.R. Woodward, SLIC (simple line interface method), Lect. Notes Phys. 59 (1976) 330.

[5] Z.S. Mao, A.E. Dukler, The motion of Taylor bubbles in vertical tubes I. A numerical simulation for the shape and the rise velocity of Taylor bubbles in stagnant and flowing liquids, J. Computat. Phys. 91 (1990) 132–142.

[6] K. Akagawa, T. Sakaguchi, Fluctuation in void ratio in two-phase flow, Bull. JSME 9 (1966) 104–120.

[7] J.U. Brackbill, D.B. Kothe, C. Zemach, A continuum method for modeling surface tension, J. Computat. Phys. 100 (1992) 335–354.

[8] E. Dayalan, Modeling CO_2 corrosion of carbon steel in pipe flow, NACE Corrosion, 1995, Paper No. 118.

[9] D.L. Youngs, Time-dependant multi material flow with large fluid distortion, in: K.W. Morton, M.J. Baines (Eds.), Numerical Methods for Fluid Dynamics, Academic Press, New York, 1982, pp. 273–285.

[10] E.T. White, R.H. Beardmore, The velocity of rise of single cylindrical air bubbles through liquids contained in vertical tubes, Chem. Eng. Sci. 17 (1962) 351–361.

[11] J. Fabre, A. Line, Modeling of two-phase slug flow, Ann. Rev. Fluid Mech. 24 (1992) 21–46.

[12] E.E. Zukoski, Influence of viscosity, surface tension and inclination angle on motion of long bubbles in closed tubes, J. Fluid Mech. 25 (1966) 821–837.

[13] D.T. Dumitrescu, Stromung an einer Luftblase im seukrechteu Rohr, Z. Angew., Math. Mech. 23 (1943) 139–149.

[14] R.M. Davies, G.I. Taylor, The mechanics of large bubbles rising through extended liquids and through liquids in tubes, Proc. Roy. Soc. Ser. A, London 200 (1950) 375–390.

[15] R.A.S. Brown, The mechanics of large bubble in tube-I. bubble velocities in stagnant liquid, Can. J. Chem. Eng. 43 (1965) 217–223.

[16] D.J. Nicklin, J.O. Wilkes, Two-phase flow in vertical tubes, Trans. Inst. Chem. Eng. 40 (1962) 61–68.

[17] P. Griffith, G.B. Wallis, Two-phase slug flow, J. Heat Transfer 83 (1961) 307–320.

[18] R. Collins, F.F. de Moraes, The motion of large gas bubble rising through liquid flowing in a tube, J. Fluid Mech. 89 (1978) 497–514.

[19] H.L. Goldsmith, S.G. Mason, The movement of single large bubbles in closed vertical tubes, J. Fluid Mech. 14 (1962) 42–58.

[20] J.B.L.M. Campos, J.R.F. Guedes de Carvalho, An experimental study of the wake of gas slugs rising in liquids, J. Fluid Mech. 196 (1988) 27–37.

[21] C. Aladjem Talvy, L. Shemer, D. Barnea, On the interaction between two consecutive elongated bubbles in a vertical pipe, Int. J. Multiphase Flow 26 (2000) 1905–1923.

[22] G.B. Wallis, One-dimensional Two-phase Flow, McGraw Hill, New York, 1969.

[23] J.D. Bugg, G.A. Saad, The velocity field around a Taylor bubble rising in a stagnant viscous fluid: numerical and experimental results, Int. J. Multiphase Flow 28 (2002) 791–803.

[24] J.D. Bugg, K. Mack, K.S. Rezkallah, A numerical model of Taylor bubbles rising through stagnant liquids in vertical tubes, Int. J. Multiphase Flow 24 (1998) 271–281.

[25] K.H. Bendiksen, On the motion of long bubbles in vertical tubes, Int. J. Multiphase Flow 11 (1985) 797–812.

[26] Z.S. Mao, A.E. Dukler, An experimental study of gas–liquid slug flow, Exp. Fluids 8 (1989) 169–182.

[27] Z.S. Mao, A.E. Dukler, The motion of Taylor bubbles in vertical tubes-II. Experimental data and simulations for laminar and turbulent flow, Chem. Eng. Sci. 46 (1991) 2055–2064.

[28] V.E. Nakoryakov, O.N. Kashinsky, B.K. Kozmenko, Experimental study of gas–liquid slug flow in a small-diameter vertical pipe, Int. J. Multiphase Flow 12 (1986) 337–355.

[29] G. Schmitt, T. Gudde, Local mass transfer coefficients and local wall shear stresses at flow disturbances, NACE Corrosion, 1995, Paper No. 102.

[30] G. Schmitt, T. Gudde, E. Strobel-Effertz, Fracture mechanical properties of CO_2 corrosion product scales and their relation to localized corrosion, NACE Corrosion, 1996, Paper No. 9.